

RSC Advances



This is an *Accepted Manuscript*, which has been through the Royal Society of Chemistry peer review process and has been accepted for publication.

Accepted Manuscripts are published online shortly after acceptance, before technical editing, formatting and proof reading. Using this free service, authors can make their results available to the community, in citable form, before we publish the edited article. This *Accepted Manuscript* will be replaced by the edited, formatted and paginated article as soon as this is available.

You can find more information about *Accepted Manuscripts* in the [Information for Authors](#).

Please note that technical editing may introduce minor changes to the text and/or graphics, which may alter content. The journal's standard [Terms & Conditions](#) and the [Ethical guidelines](#) still apply. In no event shall the Royal Society of Chemistry be held responsible for any errors or omissions in this *Accepted Manuscript* or any consequences arising from the use of any information it contains.



Journal Name

ARTICLE

Synthesis of rare-earth doped ZnO nanorods and their defect-dopant correlated enhanced visible-orange luminescence

A. Layek,^a S. Banerjee,^a B. Manna^a and A. Chowdhury^aReceived 00th January 20xx,
Accepted 00th January 20xx

DOI: 10.1039/x0xx00000x

www.rsc.org/

We report the synthesis of size controlled ZnO and rare-earth doped ZnO nanorods in the sub-10 nm diameter regime. The preferential anisotropic growth of the nanostructures along the polar c-axis leads to the formation of wurtzite phase ZnO nanorods. Photoluminescence measurements reveal enhancement of visible luminescence intensity with increasing RE³⁺ concentrations upon excitation of host ZnO into band gap. The broad visible luminescence originates from multiple intrinsic or extrinsic defects. The luminescence from RE³⁺ is enabled by energy transfer from defect centers of the host nanocrystal lattice to dopant sites. Host-guest energy transfer facilitates efficient intra-4f orbital transitions (⁵D₄ → ⁷F_J for Tb³⁺ and ⁵D₀ → ⁷F_J for Eu³⁺) related characteristic green or red emission. Interestingly, different decay rates of host defects and RE³⁺ emission transition also allow temporal control to achieve either pure green or red color. This study suggests that manipulation of defects through bottom-up technique is a viable method to modulate the energy transfer dynamics, which may help enable the future applications of ZnO-based phosphor materials in optoelectronic and multicolor emission displays.

Keywords: zinc oxide nanorods, anisotropic growth, rare-earth doping, defect luminescence, energy transfer

1. Introduction

Zinc oxide (ZnO) has attracted great research interests due to its wide and direct band gap (3.37 eV),¹ large exciton binding energy (60 meV),¹ and extensive applications in piezoelectric transducers,² chemical and gas sensors,³ optical waveguides,⁴ transparent conductive films,⁵ varistors,⁶ spintronics,⁷ and solar cell windows.^{8, 9} The decisive roles of shapes and sizes on the physical and chemical properties of semiconducting materials have already been established.¹⁰⁻¹² Thus, considerable attention has been drawn towards the design of different surface morphologies of ZnO nanostructures; e.g., nanowires,¹³ nanorods,^{14, 15} nanobelts,¹⁶ nanotubes,¹⁷ and nanohelices.¹⁸ Apart from available various morphologies, cost effectiveness, thermal and chemical stability and environmentally benign nature makes ZnO as a popular choice for optical devices.

For ZnO, there are typically two emission bands. One is centred in the UV region; the other is centred in the visible region. The UV emission is well-known to be associated with the radiative recombination of electron from conduction band with

hole from valence band. Although the origin of the visible luminescence is controversial till date, however, it has been attributed to interstitial zinc (Zn_i), oxygen vacancies (V_o), chemisorbed oxygen, copper impurities, and zinc vacancies etc.¹⁹⁻²¹ Even though the visible emission in ZnO is undesirable for near-UV emitting devices, however, most recent work by Radovanovic and co-workers has proposed an excellent model for utilization of robustly broad luminescence of ZnO in light emitting diodes.²² It fuels our interest to further explore avenues for enhancing the photoluminescence by doping Rare earth ions (RE³⁺) into ZnO. It is well known RE³⁺ emits in visible-IR region consisting of stable, sharp multiple bands at single excitation. However, it is very challenging to incorporate RE³⁺ into ZnO lattice because of giant difference in ionic radii and charge,^{23, 24} which propels intrinsic self-purification process in the host.^{25, 26} Nevertheless, attempts have been made for the generation of orange-red emission from ZnO nanomaterials by doping impurity, surface defects or trap states in the host materials.²⁷⁻²⁹ The luminescence intensities of RE³⁺ are often observed to be insufficiently low even after successful incorporation in the ZnO host.³⁰ This may be due to very rapid excitonic decay of ZnO,³¹ which inhibits direct energy transfer to RE ions; and the quenching of RE emission due to nonradiative transfer from RE³⁺ ion to ZnO host.³² Nonetheless, it remains an open question regarding the dynamics of transfer process and optimization of visible luminescence efficiency by manipulating defect-dopant interactions. Therefore, it requires

^a Department of Chemistry, Indian Institute of Technology Bombay, Mumbai 400076, India.

*To whom corresponds should be addressed. E-mail: arindam@chem.iitb.ac.in

†Electronic Supplementary Information (ESI) available: [XRD pattern showing peak shift for Tb³⁺ and Eu³⁺ doped nanorods, estimated doping concentration of rare earth ions in nanorods, PL decay and Tables listing decay parameters for rare earth doped ZnO nanorods.]. See DOI: 10.1039/x0xx00000x

further investigations in this area for better understanding and technological developments.

In this article, we report the synthesis and optical properties of RE³⁺ doped ZnO nanorods of sub-10 nm diameter regime. RE³⁺ doped nanorods show very narrow size distribution and their length depends on the growth time. The Wurtzite phase ZnO anisotropically grow along the c-axis which has high energy polar surfaces. Photoluminescence (PL) measurements reveal enhancement of visible luminescence intensity with increasing RE³⁺ concentrations upon excitation of host ZnO into band gap, indicating possible energy transfer into dopant energy level from the host. Upon excitation into ZnO band, the appearance of characteristic intra-4f orbital transitions of RE³⁺ indicates host-guest energy transfer, likely involving the ZnO defect states. Time resolved photoluminescence (TRPL) decays recorded for RE³⁺ doped ZnO nanorods in current studies are noticed to be significantly slower than undoped nanorods, which further supports that the deep defects in ZnO serve as energy traps and pave the way for effective energy transfer to doped RE³⁺ ions and their relevant light emissions. Our results indicate that chemical manipulation of defects-dopant interaction provide attractive path to achieve multicolour emission in RE³⁺-doped ZnO and may find applications in photonics, light emitting devices, and displays.

2. Experimental

2.1. Preparation of ZnO nanorods.

Undoped ZnO nanorods were synthesized by hydrothermal process in which ZnO nanoparticles were used as seed nuclei for the growth of nanorods following an experimental method prescribed by Xu *et al.*¹² In the first step, ZnO nanoparticles were synthesized by sol-gel method.³³ Briefly, a solution of potassium hydroxide (KOH) (Merck, 85 %) (~3.4 mM) in MeOH (Spectrochem, Mumbai India, 99.8%) was refluxed at 60 °C for 45 min. An ultrasonically dissolved solution of Zinc acetate dihydrate (Zn(OAc)₂ · 2H₂O) (Loba Chemie Pvt. Ltd., 98%) (~1.4 mM) in MeOH was added drop wise to the refluxing KOH solution at 60 °C. Entire mixture was rigorously stirred for 10 min to produce ZnO sols. The as prepared sol was taken in Teflon lined autoclave for the growth of undoped ZnO nanorods. The autoclave was sealed and heated at 120 °C for 4 h and then cooled at room temperature overnight. The precipitated sample was centrifuged and washed several times with Millipore water to remove any un-reacted precursors. Finally, the washed sample was dried at 50 °C in air oven for 24 h.

2.2. Preparation of RE³⁺ doped ZnO nanorods

An equimolar mixture of zinc nitrate hexahydrate (Zn(NO₃)₂ · 6H₂O) (Merck, 96 %) and hexamethylenetetramine (HMT) (C₆H₁₂N₄) (Analytical Rasayan, S D Fine-Chem Ltd., 99.5%) (1.0 mM) was dissolved in Millipore water. For RE³⁺ doping, aqueous solutions of terbium or europium nitrate pentahydrate (RE(NO₃)₃ · 5H₂O) (Sigma Aldrich 99.9 %) were added to above mixture of Zn(NO₃)₂ and HMT. RE(NO₃)₃ of 10 weight%, 20

weight%, 30 weight % and 40 weight% of Zn(NO₃)₂ were used for doping. In the second step, 60 ml of rare earth containing complex mixture was directly added to 2 ml as-prepared ZnO sols in Teflon lined autoclave. The autoclave was sealed and heated at 120 °C for 4 h and then cooled at room temperature overnight. The precipitated sample was treated in similar fashion as described for undoped ZnO nanorods.

2.3. Preparation of samples spectroscopic studies

Doped or undoped ZnO nanorods were dispersed in 3 mL of MeOH. Before solution phase spectroscopic studies, individual dispersions were sonicated for 5 min to assure the dissolution of all solid residue. For solid state PL, the dispersed nanorods were coated on a spectroscopically cleaned Si wafer.

2.4. Equipments.

Different phases in nanostructures were identified by X-ray diffraction studies using Philips powder diffractometer PW3040/60 with Cu K_α radiation (λ=1.540 Å). The chemical compositions of as-prepared samples were examined with an energy dispersive X-ray spectrometer (Oxford INCA Energy TEM 200 EDS). Transmission electron microscopic images were recorded with a high resolution transmission electron microscope (JEOL JEM 2100/ Philips CM 200) at an accelerating voltage 200 kV.

All absorption spectra were recorded with an absorption spectrophotometer (JASCO-V 530) using a quartz cuvette of 1 cm path at room temperature. All absorption spectra were recorded in the wavelength region of 250 nm to 500 nm length. Steady-state PL measurements were performed using a fluorescence spectrophotometer (Varian Carry Eclipse) with CW-Xenon lamp excitation at the excitation wavelength of 325 nm. All PL spectra were recorded in the wavelength region of 350 nm to 750 nm and the slit widths for both excitation and emission monochromator were set to 5 nm. Time delayed PL spectra were recorded with delay time 0.1 ms and gate time 5 ms. In the solid state PL experiment, a He–Cd laser source (325 nm) was used for the excitation and an Acton monochromator attached with a cooled CCD camera was used to record the spectra. Low temperature PL measurements at 10 K were also performed using the same PL setup and a closed cycle He-refrigerator.

Time-resolved luminescence studies were performed using a time correlated single photon-counting (TCSPC) system from IBH, UK to measure lifetimes in ns time range. The excitation source was a 340 nm light emitting diode with full width half maximum of 800 ps. Decays were at the emission wavelengths of 520 nm, 540 nm and 580 nm with an emission polarizer at a magic angle of 54.7°. The slit width for the emission monochromator was 8 nm. The intensity for the channel with maximum intensity was 10,000 counts. The instrument response function (IRF) was recorded using Ludox solution (Sigma Aldrich) by detecting the scattered emission at the excitation wavelength.

An iterative reconvolution method was employed to analyze all decays using IBH DAS 6.2 software. An experimental curve was fit to a program generated calculated curve, which was convoluted numerically with the instrument response function.

Decays were fit to a model of sum of two-exponentials using the IBH DAS-6 program.

$$I(t) = I(0) \sum_1^i A_i \exp\left(-\frac{t}{\tau_i}\right) \quad (1)$$

$I(t)$ and $I(0)$ are the respective luminescence intensities at time t and time zero, immediately after the excitation by the pulsed light. A_i 's are the relative contributions to the amplitude of the decay of the i^{th} species corresponding to lifetime

$$\sum_1^i A_i = 1 \quad (2)$$

The goodness of the fit to the experimental data was judged by considering the reduced χ^2 values, which should be between 0.9 and 1.2, and analyzing the randomness of the weighted residuals.

The fluorimeter which was employed for steady state PL measurements was again used for time resolved PL studies at ms time scale. All decays were recorded at the excitation wavelength of 325 nm and at emission wavelength 545 nm and 615 nm for Tb^{3+} and Eu^{3+} doped samples, respectively.

Decays were analyzed using origin by fitting to a model of sum of two-exponentials (Eq. 1) by an iterative method until fit converges. The righteousness was decided by allowing the adjacent R^2 values closer to 1 and analyzing the randomness of the residuals.

The average lifetimes (τ_{av}) were calculated using the expression

$$\tau_{av} = \frac{A_1\tau_1^2 + A_2\tau_2^2}{A_1\tau_1 + A_2\tau_2} \quad (3)$$

4. 3. Results and discussion

The seed mediated chemical route we are reporting in this paper is versatile method to prepare ZnO nanorods with ease and the diameter of nanorods can be controlled in the sub-10 nm which is scarcely reported. Moreover, the procedure also provides opportunity to dope RE^{3+} in ZnO nanorods. The structure, morphology and chemical composition of RE^{3+} doped and undoped ZnO NCs were analyzed using X-ray diffraction (XRD), Energy-dispersive x-ray spectroscopy (EDS), Transmission electron microscopy and High resolution transmission electron microscopy (HRTEM).

3.1. Characterization of ZnO and RE^{3+} -ZnO NCs

To investigate the crystallographic information of ZnO products, XRD studies were performed for both nanorods and seed nanoparticles (Fig. 1a). All XRD data could be easily indexed to the Wurtzite structure, the thermodynamically most stable form of ZnO. The anisotropic growth nanorods were

monitored by recording the XRD pattern at different time intervals of 1 h, 2 h and 4 h during the synthesis, which reveal that both nanorods and nanoparticles maintain hexagonal lattice pattern. It is observed that the full width at half maximum (FWHM) of the (002) reflection decreases faster than (100) and (101) reflections. Although all reflections become sharper with the progress of reaction, the most notable change is observed for (002) reflection plane indicating anisotropic growth along the polar c-axis of ZnO .³⁴

The XRD patterns of Tb^{3+} and Eu^{3+} doped in ZnO nanorods are shown in Fig. 1b and 1c, respectively. All the reflections can be indexed to the hexagonal ZnO and no characteristic peaks were observed for other impurities. However, the peaks were broadened compared to that of undoped sample, which may be due to the lattice mismatch, lattice distortion and strain of the crystal. It is noticeable that the XRD reflections slightly shift to lower angle (indicating expansion of the lattice) as doping concentration of RE^{3+} is increased (Fig. S1, ESI[†]). This is possibly because of the finite size effect of the doping of bigger size RE^{3+} ($r_{\text{Zn}^{2+}}=0.74 \text{ \AA}$, $r_{\text{Tb}^{3+}}=0.923 \text{ \AA}$ and $r_{\text{Eu}^{3+}}=0.947 \text{ \AA}$) which may lead to strain mediated lattice distortion. To explain the dopant-defect induced broadening of XRD line profile we performed Williamson-Hall (W-H) analysis of ZnO nanorods (Fig. S2, ESI[†]). It is known that average crystallite size and strain in the NPs can be calculated from the spectral line shape using W-H plot based on the equation

$$\beta \cos \theta_{hkl} = \frac{0.9\lambda}{D} + 4\varepsilon \sin \theta_{hkl} \quad (4)$$

where, β , θ_{hkl} , λ , D , and ε represent FWHM of the XRD reflection, Bragg's angle, wavelength of X-ray = 0.1540 nm, average particle size diameter, and strain, respectively. Assuming isotropic strain deformation model would show linear behaviour when plotted $\beta \cos \theta_{hkl}$ vs $4 \sin \theta_{hkl}$ and slope to the linear fit would indicate the strain (ε). However, we found that the W-H analysis of RE^{3+} doped nanorods display scatter data points (Fig. S2, ESI[†]). Nonlinear nature of the W-H plot clearly indicates that XRD line broadening is due to anisotropic strain in ZnO nanorods.³⁵ Qualitatively, it is noted that increase in dopant concentration induces more strain in the nanorods.

To elucidate the morphologies of the undoped and RE^{3+} doped nanorods, we performed TEM measurements. The TEM images of undoped ZnO nanorods were recorded at different time point of nanorod growth as shown in Fig. 2(a-c). It should be noted that the length of the nanorods are less than 50 nm along with many small elongated nanoparticles when the reaction was allowed to proceed for 1h (Fig. 2a). The aspect ratio, l/d (length/diameter) of nanorods grown for 2 hrs was found to be larger (Fig. 2b) than nanorods grown for 1 h. The average lengths of the nanorods grown for 4 hrs were found to be 50-100 nm with diameter ($10 \pm 2 \text{ nm}$) (Fig. 2c). It is interesting to note that the average length of the nanorods increases with the progress of reaction, however, the diameter of the nanorods remain unchanged. This observation has often been explained

by oriented attachment (OA) growth model.^{34,36} However, in our case, there is no evidence to support the 'oriented attachment' mechanism because no oriented attachment of particles has been found by HRTEM except at the primary stage of growth. Here, we propose that when a ZnO nucleus is newly formed, owing to the high energy polar surfaces, the incoming precursor molecules tend to favorably adsorb on the polar surfaces in order to minimize the total energy of the system.³⁷ However, after adsorption of one layer of precursor molecules, the polar surface transforms into another polar surface with inverted polarity, *i.e.*, a Zn²⁺-terminated surface changes into an O²⁻-terminated surface, or vice versa. Repetition of this process over time leads to a fast growth along the [0001] direction resulting in nanorod formation.

In Fig. 2d, the HRTEM image of the ZnO nanorods shows clear lattice fringes with the distance between two parallel lattices was measured to be ~ 0.26 nm, corresponding to the (002) crystal planes, consistent with XRD pattern. From all the above observations, it is proved beyond doubt that anisotropic growth favourably along polar c-axis of ZnO is responsible for the formation 1D-nanorods.

The TEM micrographs of RE³⁺ doped nanorods (grown for 4 hrs) are shown in Fig. 3. The Tb³⁺ doped nanorods are depicted in Fig. 3a while Eu³⁺ doped nanorods are shown in Fig. 3b. The average length of Tb³⁺ doped nanorods was found to be in the range 50-80 nm whereas for Eu³⁺ doped nanorods the average length was 40-60 nm. Although it is well known that presence of dopant impurity in the reaction mixture might inhibits the NC nucleation and growth, however, the reason for such variation of length between Tb³⁺ and Eu³⁺ doped nanorods is hitherto unknown to us. Nevertheless, there is no noticeable variation in the average diameter (10 ± 2 nm) of RE³⁺ doped nanorods and undoped ZnO nanorods. From the HRTEM images in Fig. 3c (Tb³⁺ doped) and Fig. 3d (Eu³⁺ doped), this is evident that the doped nanorods are single crystalline in nature with clear lattice fringes where distance between parallel planes is ~ 0.26 nm. Moreover, RE doped ZnO also grow anisotropically along the polar c-axis, similar to the undoped ZnO nanorods.

Fig. 4 displays the representative EDS graphs where distinct signature peaks related to RE³⁺ (Tb³⁺ in Fig. 4a and Eu³⁺ in Fig. 4b) are observed. From this elemental analysis, it was found that the amount of incorporated Tb³⁺ and Eu³⁺ ions increases concomitantly with increasing their respective RE³⁺ precursor concentration added to ZnO sol during nanorods growth. We also observed that that Tb³⁺ has relatively higher propensity to be incorporated into ZnO nanorods than that of Eu³⁺, although their precursor concentrations were same (Fig. S3, ESI[†]). It should be noted that the actual amount of RE³⁺ doped in the NRs were estimated from five point averages for each samples.

3.2. Spectroscopic properties of nanorods

Optical absorption spectra of undoped and RE³⁺ ion doped ZnO nanorods are shown in Fig. 5. The clear blue shift of excitonic absorption maxima with RE³⁺ doping denotes band

gap enhancement due to inhibited growth of the nanorods with increasing dopant concentration in the nanocrystal host. In the insets of Fig. 5, it is shown that the excitonic absorption maxima of undoped nanorods blue shift from 368 nm to 356 nm (355 nm) for Tb³⁺ (Eu³⁺) doped nanorods. It is well known that dopant ions on the nanocrystal surfaces may inhibit growth and hence smaller size which results in band gap.³⁸ However, there is no significant size variation is observed with increasing doping concentration. Moreover, diameter of the nanorods much larger than the exciton Bohr radius and hence size dependent quantum confinement can be ruled out. Recently, Sharma *et al.* reported band gap enhancement as a consequence of Tb³⁺ doping in the sub-surface regions of ZnO nanoparticles, due to which hydrodynamic compressive strain arises in the NCs.^{39,40} The dopant induced strain is likely to be responsible for blue shift of absorption peak in RE³⁺ doped ZnO nanorods. It is in good agreement with the W-H analysis where it shows RE³⁺ doping induces anisotropic strain in ZnO nanorods. It is therefore, reasonable to believe that this type of stress/strain effect may also be responsible for the blue-shift of the excitonic transition of RE³⁺ doped ZnO nanorods.

The solution phase PL spectra (Fig. 6) of both undoped and doped ZnO nanorods show very sharp UV emission with a maximum at ~ 380 nm. The narrow UV emission (FWHM < 25 nm) has earlier been attributed to the radiative annihilation of excitons or near band edge (NBE) emission.^{41, 42} The sharp feature of the of the UV emission also gives indirect signature of narrow size distribution of the nanorods,⁴³ which is in good agreement with TEM observations (Fig. 2 and 3). Interestingly, it is noted that although the excitonic absorption maxima blue shift with increasing doping content (Fig. 6), there is no significant shift (± 2 nm) in NBE maxima.

A broad visible PL band (Fig. 6) is noticed in the wavelength region of 500 nm 750 nm. Similar inherently broad visible band is usually observed for ZnO crystal and attributed to deep level defects within the crystal such as vacancies and interstitials of oxygen and zinc.⁴⁴⁻⁴⁶ Undoped ZnO rods have feeble emission in similar visible wavelength region. However, intensity related to defect emission is increased with increasing impurity doping. The doping induced enhancement of visible luminescence intensities of nanorods may be attributed to more defects generated due to RE³⁺ ions incorporation in the ZnO lattice and energy transfer from ZnO defect states to the guest RE³⁺ ions. Rare-earth incorporated defects are either due to their lattice mismatch or creating oxygen vacancy owing to their charge imbalance in the Zn²⁺ sites. Although steady-state PL does not show transitions related to RE³⁺ ions, however, time delayed PL (Fig. 6c-d) exhibits characteristic intra-4f transitions (⁵D₄ \rightarrow ⁷F_j) for Tb³⁺ and (⁵D₀ \rightarrow ⁷F_j) Eu³⁺ ions present inside the ZnO host. The emission spectra for Tb³⁺ doped ZnO consist of four main lines at 488 nm (⁵D₄-⁷F₆), 543 nm (⁵D₄-⁷F₅), 586 nm (⁵D₄-⁷F₄), and 620 nm (⁵D₄-⁷F₃) under 325 nm excitation.^{47, 48} In case of Eu³⁺-doped ZnO nanorods, five relatively narrow emission peaks are observed at 583, 592, 615, 650, and 706 nm due to ⁵D₀ \rightarrow ⁷F_{0,1,2,3,4} intra-4f transitions upon excitation at 325 nm.

Therefore, from these combined results it is very likely that energy transfer from host ZnO defect levels to RE³⁺ is responsible for the enhanced visible luminescence of nanorods. Time-resolved PL measurements (*vide ante*) further confirm defect mediated host-guest energy transfer processes.

Solid state PL spectra were recorded at different temperature ranging from 10 K to 300 K. The narrow UV emission band maximum (~370 nm) at 10 K gradually red-shifts with increase of temperature (Fig. 7a) and become a relatively broader emission at ca. ~380 nm). The red shift of the UV band maxima is associated with simultaneous decrease of PL intensity with increase of temperature (Fig. 7a). Earlier Zhao *et al.* has observed similar temperature dependent red-shift if the UV PL band for ZnO nanowires grown on sapphire substrates.⁴⁹ The sharp UV PL band at ca. 370 nm which was observed at 10 K is assigned to impurity related exciton, most likely donor-bound exciton. The intensity of the band due to donor-bound exciton decreases with increase of temperature and it red-shifts gradually due to decrease of band-gap energy. At higher temperature the contribution due to donor-bound exciton minimizes. The broad band with maximum at 380 nm observed at room temperature is related to the transition due to free-to-bound exciton, which survives at room temperature. Current temperature dependent PL study is in good agreement with the results reported by Zhao *et al.*⁴⁹

The characteristic PL emission originating from Tb³⁺ related intra-4f transitions are observed in solid state PL measurement for Tb³⁺-doped ZnO nanorods (Fig. 7b) at 325 nm excitation. The emission spectra for Tb³⁺ doped ZnO consist of four main lines at 488 nm, 543 nm, 586 nm, and 620 nm under 325 nm laser excitation (*vide infra*).⁴⁷ These sharp signatures of intra-4f transitions appear along with broad defect luminescence of ZnO. The lower intensity visible emission observed at room temperature under evacuated conditions indicates that adsorbed solvents (or water or other labile groups), surface hydroxyl groups are responsible for the intense defect emission (Fig. 7a), in addition to defects induced by Tb³⁺ ions. It should be noted that experimental excitation wavelength of 325 nm does not correspond to any particular intra-4f excitation of Tb³⁺, but higher energy near band-gap excitation of ZnO NCs. The emission due to intra-4f transitions indicates excited state energy transfer mechanism as proposed by Wang *et al.*⁵⁰ The mechanism proposes the band-gap excitation of carriers is followed by the relaxation of carriers to the band edge of conduction band and valence band. After that, carriers are either trapped in the defects or undergo radiative transition. The trapped excitons transfer energy to the excited states of RE³⁺ resulting intra-4f emission. Recently Leung and co-workers have shown a cascade energy transfer model in 1, 10-Phenanthroline (phen) (non-emissive) functionalized Eu-doped ZnO nanostructure where phen act as potential exciton trap acceptor from ZnO conduction band (CB) and subsequently energy of the excited triplet state of phen is efficiently transferred to the near resonant states of Eu³⁺ in ZnO host.⁵¹ From our results and evidences available in the literature, it is

therefore reasonable proposition that RE³⁺ emission happens via sensitize activation pathway and not due to direct excitation of the luminescent centres in RE³⁺ doped ZnO nanorods.

To analyze the charge carrier dynamics for better understanding of the excited state energy transfer from ZnO to RE³⁺ ions, time resolved PL measurements were carried out. PL decays were recorded at the excitation of 290 nm, far away from the lowest energy excitation maxima of Tb³⁺ (349 nm)⁴⁸ and Eu³⁺ (414 nm).⁵⁰ Emission decay were collected at the emission wavelength ca. 545 nm for Tb³⁺ with maximum intensity (Fig. 6c) or 615 nm for Eu³⁺ (Fig. 6d). PL decays traces were observed to decay completely in 1-1.5 ms time range (Fig. S4 and S4 in ESI[†]). Two lifetimes were well recovered from individual decays recorded for Tb³⁺-doped nanorods (Table S1, ESI[†]): Two recovered lifetime vary within the range of (80-90) μs and (380-390) μs. Earlier, PL decays of undoped nanorods were reported to decay within 50 ns.⁵² Decay profiles and temporal parameters for Tb³⁺ doped ZnO nanorods are independent of doping content (Fig. S4 and Table S1 in ESI[†]). Thus, recovered μs lifetimes in present study are related neither to intrinsic defects of ZnO nanorods, nor to Tb³⁺ doping related defects. Similar results were also achieved for Eu³⁺ doped in ZnO nanorods (see ESI[†], Fig. S5 and Table S2), where two recovered lifetimes vary within (50-70) μs and (270-300) μs. Both μs lifetimes recovered from same decay are related to RE³⁺ doped in ZnO nanorods. Actually, the differences of lifetimes arise due to variation of distribution of RE³⁺ located at the surface or deeper inside the nanorods. The luminescence lifetimes are related to ⁵D₄-⁷F₅ transition for Tb³⁺ and ⁵D₀-⁷F₂ transition for Eu³⁺, which is achieved at near band-gap excitation. Thus recovery of RE³⁺ lifetimes from the decay at near band-gap excitation supports the mechanism of excited state energy transfer from ZnO host to doped RE³⁺ ions. The excited carriers in the band edge relaxes through several possible mechanisms e.g., radiative or nonradiative recombination, multiphonon emission, or fast trapping of carriers to the defect states.⁵⁰ Depopulation of carriers trapped in the defects may occur through radiative or nonradiative recombination, multiphonon emission and energy transfer to RE³⁺ ions.^{50, 53} Herein, the chemical methodology adopted to synthesize RE³⁺ doped nanorods generates defects which likely act as the energy storage trapping carriers and gradually transfers energy to dopant sites.

To reveal the photophysics of charge carriers of ZnO host, time correlated single photon counting (TCSPC) experiments were performed at nanosecond time resolution. The PL intensity for undoped nanorods was too low for TCSPC measurements. Therefore decays were recorded for Tb³⁺ (40 weight %) doped nanorod. Earlier, Layek *et al.* have reported higher intensity for the visible PL band for ZnO nanorods synthesized following same procedure but at lower temperature (90 °C).⁵² Temporal parameters reported by Layek *et al.* were considered for undoped nanorods for comparison with doped nanorods. PL decays recorded for RE³⁺ doped nanorods in current studies are noticed to be significantly

slower than undoped nanorods.⁵² PL decays recorded for Tb³⁺-doped nanorods at the emission wavelengths of 540 nm and 580 nm are almost overlaid, while the PL decay recorded at the emission wavelength ca. 520 nm is faster than other two decays (Fig. 8a). Two lifetimes (τ_1 and τ_2) recovered from each PL decays are simultaneously lengthened at emission wavelength ca. 540 nm or 580 nm compare to the emission wavelength of 520 nm (Table S1). Average lifetime ($\langle\tau\rangle$) also become longer at higher emission wavelengths. Previously Rakshit *et al.* has studied spectrally resolved dynamics of oleate capped ZnO:MgO NCs.⁵⁴ Time resolved emission spectra (TRES) were constructed in the same wavelength region of broad visible defect emission was resolved into two bands.⁵⁴ The band in the region of 480 nm to 520 nm appears at shorter time scale and red shifts with time. Second band appears at longer wavelength and evolves with time at the expense of band at shorter wavelength. The decay at the emission wavelength of 520 nm is faster as it is related to the recombination of electron and hole trapping in the deep defects, while the decay at the emission wavelength of 540 nm (or higher) is related to slow recombination of hole and trap states. The results of low temperature PL measurements (Fig. 7b) show the signatures of intra-4f transition of Tb³⁺ at the wavelength region of 540 nm or 580 nm, which is absent at 520 nm. Thus, the decay at the emission wavelength of 540 nm or 580 nm has further contribution due to intra-4f orbital transition of Tb³⁺ which relates μ s lifetime. Thus, slower carrier recombination process and intra-4f transition of Tb³⁺ are probably responsible for the delaying the decay at the emission wavelength of 540 nm or 580 nm relative to 520nm (Fig. 8b). However, defect mediated host-guest energy transfer dynamics still remains elusive and require further studies.

Conclusions

In summary, we synthesized rare-earth RE³⁺ doped ZnO nanorods in the diameter regime 10-12 nm by simple wet chemical technique. We showed that the formation of 1D RE³⁺ doped ZnO nanorods is the manifestation of "oriented attachment" growth kinetics evidenced with XRD and TEM measurements. Energy dispersive x-ray spectroscopy shows the incorporation of RE³⁺ ions into the ZnO host. Absorption measurement reveals that incorporation of RE³⁺ ions induces lattice strain which causes a shift in the excitonic absorption band toward higher energy. Room temperature solution phase PL with 325 nm xenon light excitation shows narrow (FWHM < 25 nm) and strong UV luminescence along with broad visible emission due to multiple deep level defects. We showed that with increasing RE³⁺ dopant concentrations visible luminescence intensity further increases. It is likely that there are more strain induced defects created due to size disparity between Zn²⁺/RE³⁺ ions and defect mediated energy transfer from host ZnO to guest dopant ions. Although, solution phase PL measurements do not show any signature emission band from RE³⁺, however, solid state PL, measurements under 325 laser excitation clearly show characteristic intra-4f transition lines of RE³⁺ ions. Moreover, time-delayed PL measurements

exhibits intra- 4f orbital transition for Tb³⁺ (Eu³⁺) related characteristic green (red) emission. Time resolved experiments further provide evidences that intrinsic or extrinsic defects act as energy trapping centres which pave way for energy transfer from deep defects in host ZnO to RE³⁺ ions. Therefore, controlling ZnO nanorod dimensions, defect density, and dopant concentrations allows for modulation of luminescence colour and intensity. The present study indicates that via defect engineering, rare-earth-doped ZnO nanorods may find avenues for potential applications in optoelectronic and multicolour emission display devices.

Acknowledgements

This work was supported by CSIR (India) grant to AC (Scheme: 80(0070)/08/EMR-II) and IRCC IIT Bombay. We would like to thank Centre for Research in Nanotechnology and Science (CRNTS) for TEM facility, and Departments of Chemistry, IIT Bombay for usage of central facility instruments. A.L. especially thanks Prof. B. P. Singh and S. Dhar for providing solid state PL measurement facility and their valuable comments.

Notes and references

1. M. H. Huang, S. Mao, H. Feick, H. Yan, Y. Wu, H. Kind, E. Weber, R. Russo and P. Yang, *Science*, 2001, **292**, 1897.
2. T. Shiosaki and A. Kawabata, *Appl. Phys. Lett.*, 1974, **25**, 10.
3. T.-J. Hsueh, C.-L. Hsu, S.-J. Chang and I. C. Chen, *Sensor. Actuator. B: Chem.*, 2007, **126**, 473.
4. C.-L. Jia, K.-M. Wang, X.-L. Wang, X.-J. Zhang and F. Lu, *Opt. Express*, 2005, **13**, 5093.
5. J.-H. Lee, K.-H. Ko and B.-O. Park, *J. Cryst. Growth*, 2003, **247**, 119.
6. A. T. Yu and A. B. Glot, *J. Phys. D: Appl. Phys.*, 2012, **45**, 465305.
7. L. Vayssieres, *Adv. Mater.*, 2003, **15**, 464.
8. E. Galoppini, J. Rochford, H. Chen, G. Saraf, Y. Lu, A. Hagfeldt and G. Boschloo, *J. Phys. Chem. B*, 2006, **110**, 16159.
9. G. Kron, U. Rau and J. H. Werner, *J. Phys. Chem. B*, 2003, **107**, 13258.
10. C. Burda, X. Chen, R. Narayanan and M. A. El-Sayed, *Chem. Rev.*, 2005, **105**, 1025.
11. I. Shalish, H. Temkin and V. Narayanamurti, *Phys. Rev. B*, 2004, **69**, 245401.
12. F. Xu, Y. Lu, Y. Xie and Y. Liu, *J. Phys. Chem. C*, 2009, **113**, 1052.
13. P. Yang, H. Yan, S. Mao, R. Russo, J. Johnson, R. Saykally, N. Morris, J. Pham, R. He and H. J. Choi, *Adv. Funct. Mater.*, 2002, **12**, 323.
14. X. Wang, J. Song, P. Li, J. H. Ryou, R. D. Dupuis, C. J. Summers and Z. L. Wang, *J. Am. Chem. Soc.*, 2005, **127**, 7920.
15. Z. W. Pan, Z. R. Dai and Z. L. Wang, *Science*, 2001, **291**, 1947.
16. Z. L. Wang, *J. Mater. Chem.*, 2005, **15**, 1021-1024.
17. L. Vayssieres, K. Keis, A. Hagfeldt and S.-E. Lindquist, *Chem. Mater.*, 2001, **13**, 4395.

18. P. X. Gao, Y. Ding, W. Mai, W. L. Hughes, C. Lao and Z. L. Wang, *Science*, 2005, **309**, 1700.
19. D. C. Look, J. W. Hemsky and J. R. Sizelove, *Phys. Rev. Lett.*, 1999, **82**, 2552.
20. F. Tuomisto, V. Ranki, K. Saarinen and D. C. Look, *Phys. Rev. Lett.*, 2003, **91**, 205502.
21. D. C. Look, G. C. Farlow, P. Reunchan, S. Limpijumngong, S. B. Zhang and K. Nordlund, *Phys. Rev. Lett.*, 2005, **95**, 225502.
22. A. Layek, P. C. Stanish, V. Chirmanov and P. V. Radovanovic, *Chem. Mater.*, 2015, **27**, 1021.
23. S.-M. Liu, F.-Q. Liu, H.-Q. Guo, Z.-H. Zhang and Z.-G. Wang, *Phys. Lett. A*, 2000, **271**, 128.
24. Y. Yang, H. Lai, C. Tao and H. Yang, *J. Mater. Sci.: Mater. Electron.*, 2010, **21**, 173.
25. G. M. Dalpian and J. R. Chelikowsky, *Phys. Rev. Lett.*, 2006, **96**, 226802.
26. G. Galli, *Nature*, 2005, **436**, 32.
27. Y.-K. Park, J.-I. Han, M.-G. Kwak, H. Yang, S.-H. Ju and W.-S. Cho, *Appl. Phys. Lett.*, 1998, **72**, 668.
28. Y.-K. Park, J.-I. Han, M.-G. Kwak, H. Yang, J. Sung-Hoo and W.-S. Cho, *J. Lumin.*, 1998, **78**, 87.
29. X. Zeng, J. Yuan, Z. Wang and L. Zhang, *Adv. Mater.*, 2007, **19**, 4510.
30. Y. N. Hayashi, H.; Uchida, T.; Noguchi, T.; and Ibuki, S. , *Appl. Phys. Lett.*, 1995, **34**, 1878.
31. S.-K. Lee, S. L. Chen, D. Hongxing, L. Sun, Z. Chen, W. M. Chen and I. A. Buyanova, *Appl. Phys. Lett.*, 2010, **96**, 083104.
32. V. X. Quang, N. Q. Liem, N. C. Thanh, T. van Chuong and L. T. le Thanh, *Phys. Status Solidi (a)*, 1983, **78**, K161.
33. A. Layek, G. Mishra, A. Sharma, M. Spasova, S. Dhar, A. Chowdhury and R. Bandyopadhyaya, *J. Phys. Chem. C*, 2012, **116**, 24757.
34. C. Pacholski, A. Kornowski and H. Weller, *Angew. Chem. Int. Ed.*, 2002, **41**, 1188.
35. P. K. Giri, S. Bhattacharyya, Dilip K. Singh, R. Kesavamoorthy, B. K. Panigrahi, and K. G. M. Nair, *J. Appl. Phys.*, 2007, **102**, 093515.
36. R. L. Penn and J. F. Banfield, *Science*, 1998, **281**, 969-971.
37. M. Ethayaraja, K. Dutta, D. Muthukumaran and R. Bandyopadhyaya, *Langmuir*, 2007, **23**, 3418.
38. T. Wang, A. Layek, I. D. Hosein, V. Chirmanov and P. V Radovanovic, *J. Mater. Chem. C*, 2014, **2**, 3212.
39. A. Sharma, S. Dhar, B. P. Singh and T. Kundu, *Solid State Commun.*, 2011, **151**, 1885.
40. A. Sharma, S. Dhar, B. P. Singh, T. Kundu, M. Spasova and M. Farle, *J. Nanopart. Res.*, 2012, **14**, 1.
41. M. H. Huang, Y. Wu, H. Feick, N. Tran, E. Weber and P. Yang, *Adv. Mater.*, 2001, **13**, 113.
42. S. Monticone, R. Tufeu and Kanaev, *J. Phys. Chem. B*, 1998, **102**, 2854.
43. L. Guo, Y. L. Ji, H. Xu, P. Simon and Z. Wu, *J. Am. Chem. Soc.*, 2002, **124**, 14864.
44. A. van Dijken, E. A. Meulenkaamp, D. Vanmaekelbergh and A. Meijerink, *J. Lumin.*, 2000, **90**, 123.
45. A. Layek, S. De, R. Thorat and A. Chowdhury, *J. Phys. Chem. Lett.*, 2011, **2**, 1241.
46. B. Panigrahy, M. Aslam, D. S. Misra, M. Ghosh and D. Bahadur, *Adv. Funct. Mater.*, 2010, **20**, 1161.
47. S. Ji, L. Yin, G. Liu, L. Zhang and C. Ye, *J. Phys. Chem. C*, 2009, **113**, 16439.
48. Y. L. L. Yang, Y. Xiao, C. Ye, L. Zhang, *Chem. Lett.*, 2005 **34**, 828.
49. Q. X. Zhao, M. Willander, R. E. Morjan, Q.-H. Hu and E. E. B. Campbell, *Appl. Phys. Lett.*, 2003, **83**, 165.
50. D. Wang, G. Xing, M. Gao, L. Yang, J. Yang and T. Wu, *J. Phys. Chem. C*, 2011, **115**, 22729.
51. J. S. Kang, Y. K. Jeong, J. G. Kang, L. Zhao, Y. Sohn, D. Pradhan and K. T. Leung, *J. Phys. Chem. C*, 2015, **119**, 2142.
52. A. Layek, B. Manna and A. Chowdhury, *Chem. Phys. Lett.*, 2012, **539–540**, 133.
53. M. Zhong, G. Shan, Y. Li, G. Wang and Y. Liu, *Mater. Chem. Phys.* 2007, **106**, 305.
54. S. Rakshit and S. Vasudevan, *J. Phys. Chem. C*, 2008, **112**, 4531.

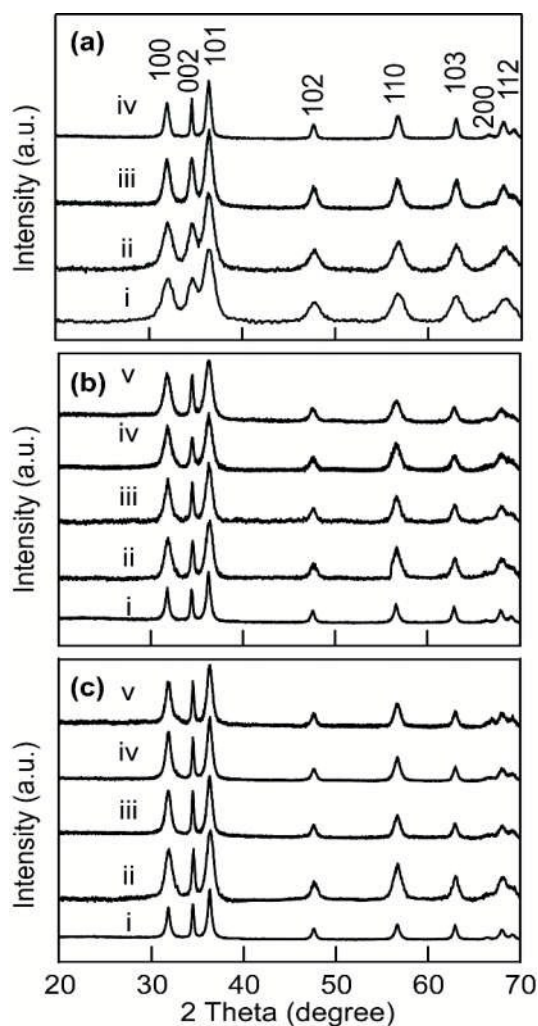


Fig. 1 (a) XRD patterns of (i) spherical ZnO nanoparticles and ZnO nanorods grown for different time durations (ii) 1 h, (iii) 2 h, and (iv) 4 h, respectively. XRD patterns of ZnO nanorods doped using different concentrations of Tb^{3+} precursor and (c) Eu^{3+} . XRD patterns in panel b and c are related to NCs synthesized in the reaction media with Tb^{3+} or Eu^{3+} precursors concentration (i) 0, (ii) 10, (iii) 20, (iv) 30, and (v) 40 weight % respectively.

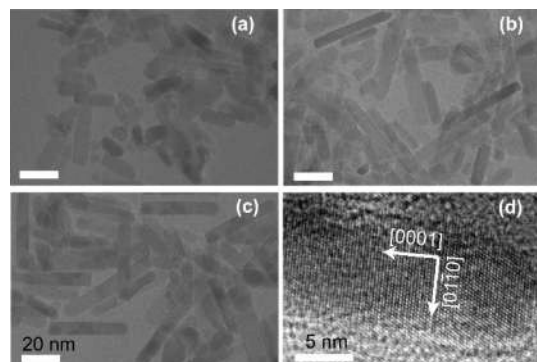


Fig. 2 TEM images of ZnO nanorods allowed to grow for time duration (a) 1 h, (b) 2 h, and (c) 4 h, respectively. (d) The HRTEM image of ZnO nanorods shows lattice fringes with diameter ~ 10 nm. Arrowheads indicates anisotropic growth of undoped nanorods occurring along [0001] direction.

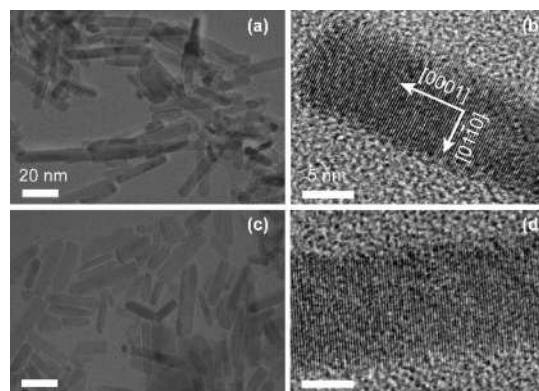


Fig. 3 TEM images of (a) Tb^{3+} and (c) Eu^{3+} doped ZnO nanorods are shown while (b) and (d) correspond to their respective HRTEM images. From HRTEM images it has been found that the inter planer distance is ~ 2.6 Å and anisotropic growth of doped nanorods is occurring along the polar c-axis or [0001] direction.

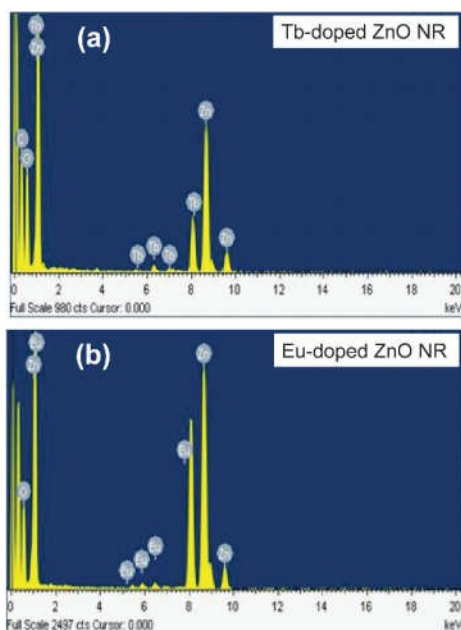


Fig. 4 Typical EDS micrograph of (a) Tb^{3+} -doped and (b) Eu^{3+} -doped ZnO nanorods.

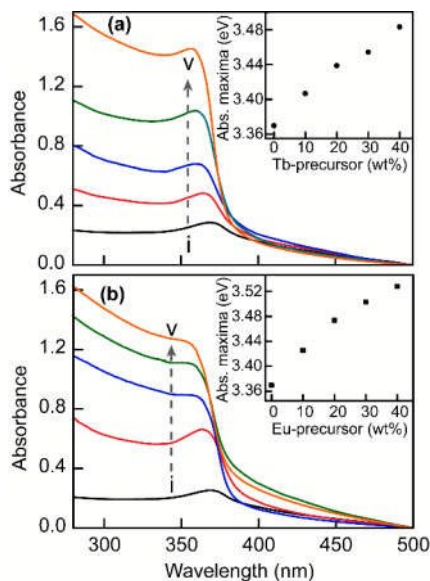


Fig. 5 Steady-state optical absorption spectra of (a) Tb^{3+} and (b) Eu^{3+} doped ZnO nanorods. The numbers in parenthesis denote added concentrations of Tb^{3+} or Eu^{3+} precursors (weight %) for doping, Arrowheads indicate the blue shift of the absorption maxima with the increase of doping content.

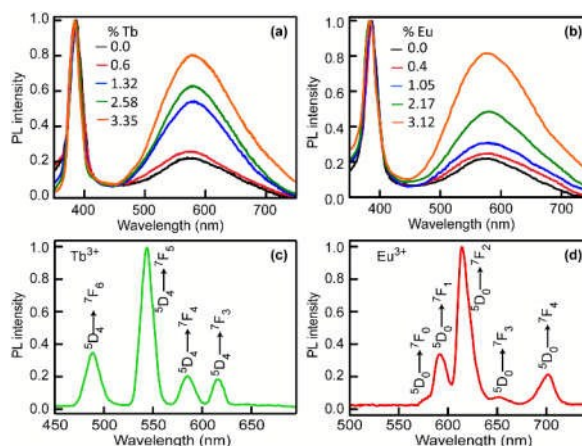


Fig. 6 PL spectra recorded for RE^{3+} doped ZnO nanorods synthesized using different concentrations (atom%) of (a) Tb^{3+} and (b) Eu^{3+} precursors. All spectra are normalized at respective wavelengths of UV PL band maxima. The gradual increase of visible PL intensity with increase of RE^{3+} doping content is indicated by arrowheads. (c-d) Time delayed PL spectra are shown for Tb^{3+} and Eu^{3+} doped ZnO nanorods, respectively. Time delayed PL spectra display characteristic intra-4f orbital transitions in both cases. All spectra were recorded at the excitation wavelength of 325 nm.

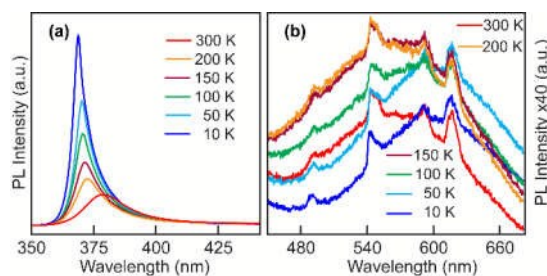


Fig. 7 Temperature dependent solid state PL measurements for ZnO nanorods doped with 3.3 atom % Tb precursor; (a) NBE emission intensity of ZnO increases and blue shifts to higher energy with decrease in temperature; (b) Visible PL spectra due to distinct intra-4f transition lines related to Tb^{3+} in ZnO nanorods with decrease in temperature. All spectra were recorded at the excitation wavelength of 325 nm.

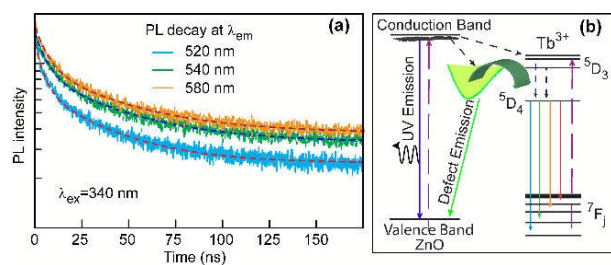


Fig. 8 (a) PL decay of Tb^{3+} doped ZnO nanorods using 40 weight% Tb precursors. Decays were recorded at the excitation wavelength of 340 nm and at the emission wavelength of 520 nm (blue trace), 540 nm (green trace) and 580 nm (orange trace); (b) Schematic illustration of intra-4f orbital transition energy lines in Tb^{3+} -doped ZnO nanorods.

TOC Graphic

Rare-earth doped sub-10 nm diameter ZnO nanorods show defect-dopant assisted enhanced visible-orange luminescence and also display multicolour rare-earth emission.

